JOURNAL OF AIRCRAFT
Vol. 45, No. 5, September–October 2008

Airbrake-Induced Fin-Buffet Loads on Fighter Aircraft

Christian Breitsamter* and Arne Schmid†
Technische Universität München, 85747 Garching, Germany

DOI: 10.2514/1.33969

The investigations presented focus on the influence of an airbrake wake on the buffet characteristics of the vertical tail (fin) of a single-finned high-agility aircraft. The study uses a detailed wind-tunnel model of a delta–canard configuration fitted with a centerline air brake located upstream of the fin. The results include turbulent flowfield data based on hot-wire anemometry as well as unsteady fin pressures measured with surface-integrated sensors. The tests are conducted in the low-speed region at a Reynolds number of 1×10^6 and at angles of attack of 0 to 30 deg considering airbrake deflections of 45 and 60 deg. Flow separation at the airbrake side edges and upper edge results in a highly turbulent airbrake wake. The corresponding region of high turbulence intensities impinges on the fin, with the turbulence levels increasing with angle of attack. This increase is caused by the inboard movement and expansion of the wing and canard vortices compressing the airbrake wake in the fin region. At low angles of attack, the airbrake wake exhibits distinct concentrations of turbulent kinetic energy at characteristic frequencies attributed to airbrake vortex shedding. Increasing the angle of attack, the airbrake side-edge vortices roll up to form leading-edge vortices associated with a periodic breakdown wake. At high angles of attack, the fin is also subject to quasi-periodic loads evoked by induction of the burst wing leading-edge vortices.

Nomenclature

$\bar{c}_p$	=	time-averaged pressure coefficient
$\hat{c}_p$	=	amplitude spectrum of pressure coefficient, $\sqrt{2S_{c_p}\Delta k U_\infty / l_\mu}$
c'_p	=	fluctuation part of c_p
$c_{p_{\text{rms}}}$	=	rms value of c'_p, $\sqrt{\overline{c'^2_p}}$
$c_p(t)$	=	pressure coefficient, $(p(t) - p_\infty)/q_\infty$
c_r	=	root chord, m
d_{AB}	=	airbrake width, m
f	=	frequency, Hz
l_C	=	characteristic length, m
l_μ	=	wing mean aerodynamic chord, m
k	=	reduced frequency, $f l_\mu / U_\infty$
$p(t)$, p_∞	=	pressure, ambient pressure, Pa
q_∞	=	freestream dynamic pressure, Pa
Re_{l_μ}	=	Reynolds number, $U_\infty l_\mu / \nu$
S_{c_p}	=	pressure spectral density, 1/Hz
s	=	wing semispan, m
U_C, U_∞	=	characteristic velocity, freestream velocity, m/s
v'	=	lateral velocity fluctuations, m/s
v_{rms}	=	rms value of v', $\sqrt{\overline{v'^2}}$, m/s
α	=	aircraft angle of attack, deg
η_{AB}	=	airbrake deflection angle, deg
Λ	=	aspect ratio
λ	=	taper ratio
ν	=	kinematic viscosity, m^2/s
φ	=	leading-edge sweep, deg

Subscripts

C, W, F	=	canard, wing, fin
dom	=	dominant

Received 10 August 2007; revision received 24 April 2008; accepted for publication 25 April 2008.

*Chief Scientist, Institute of Aerodynamics. Associate Fellow AIAA.
†Research Engineer, Institute of Aerodynamics.

I. Introduction

THE flight envelope of highly maneuverable aircraft is limited by dynamic aeroelastic problems such as buffeting, buzz, and flutter [1–3]. The fin-buffeting problem is an especially critical issue for high-performance fighter aircraft equipped with twin vertical tails [4–6], but single-fin configurations are also affected [3,7]. The associated unsteady aerodynamic loads occur mainly at high angles of attack and are attributed to the highly turbulent flow caused by burst leading-edge vortices [8]. Strong large-scale vortices are shed at slender-wing geometries such as delta-wing planforms, strakes, or leading-edge extensions. Leading-edge vortices in a fully developed stable stage significantly improve maneuvering capabilities because of additional lift and an increase in the maximum angle of attack [9,10]. However, leading-edge vortices are subject to breakdown at high angles of attack [8,11]. The occurrence and movement of vortex breakdown is mainly influenced by swirl level and an external adverse pressure gradient, which in turn depend on wing leading-edge sweep and angle of attack. The breakdown flow leads to high turbulence levels, and specific instability mechanisms develop, resulting in narrowband unsteady aerodynamic forces [12–14]. Thus, the vertical-tail structure is excited in its natural frequencies, mainly in its first bending and torsion mode. This excitation leads to increased fatigue loads that reduce service life and raise maintenance costs, respectively.

Numerous studies concentrated on the fin-buffeting problem, carefully analyzing the corresponding vortex-flow structures based on wind-tunnel tests of generic and small-scale models [14–17] as well as of full-scale configurations [18]. These experiments are supplemented by flight tests [3,6] and detailed numerical flow simulations [19–21]. Thus, the fluid–structure interaction of vortex breakdown with a fin involves the following phenomena (Fig. 1): the time-averaged breakdown location depending on swirl level and the external adverse pressure gradient set by the recompression at the wing trailing-edge and/or by the blockage of the fin, the helical-mode instability of the breakdown flow [12,13], quasi-periodic oscillations of the breakdown location [13], distortion of the incident vortex and vortex splitting [15], unsteady flow separation at the fin leading edge, and possible coupling between the separated fin flow and/or fin elastic deflections with oscillations of the breakdown location. Among these, the dominant phenomenon causing fin buffeting is the quasi-periodic loading on the fin due to the helical-mode instability of the leading-edge vortex-breakdown flow.

Consequently, the fatigue life of the fin airframe is reduced by the impact of the buffet loads, and the angle-of-attack envelope may be limited, to not exceed dynamic load limitations. To describe the

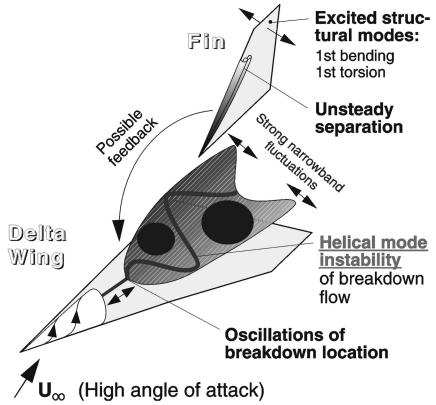

Fig. 1 Phenomenology of fin buffeting induced by the flow of burst leading-edge vortices.

fin-buffet environment and to predict the corresponding unsteady loads, design methods have been developed based on wind-tunnel tests and semi-empirical approaches [4,6]. Also, several methods have been proposed to counteract the buffeting problem, including both structural and aerodynamic means. Such methods focus on modifying structural properties such as stiffness and damping [22], passive or active flow control aimed to avoid a direct impact of the burst vortex flow [23], and methods of active vibration alleviation [24–26]. The reduction of the high structural dynamic loads would extend the fin service life and enhance the aircraft maneuverability by a possible increase of the allowable maximum angle of attack.

In addition to the unsteady effects associated with burst wing leading-edge vortices, drag-producing elements such as deflected spoilers or air brakes are also a source of turbulent wakes creating high fluctuation levels. The impact of such a wake can again cause severe structural dynamic loads on horizontal and vertical stabilizers. In particular, periodic vortex shedding at an upstream-located air brake may lead to an unsteady pressure loading on the fin (Fig. 2). The superposition of unsteady loads due to wing vortex-breakdown flow and airbrake wake could result in critical dynamic peak loads. There are extensive investigations dealing with the turbulent wake of bluff bodies [27–30], but the studies do not address the effects in combination with lifting surfaces creating leading-edge vortices.

Therefore, the present investigation is aimed to analyze the turbulent velocity fields downstream of a deflected air brake together with the induced fin surface pressures, concentrating on a delta-wing–canard configuration. Vortex shedding at the airbrake side edges and the upper edge can result in strong periodic fluctuations impinging on the fin. The main investigation parameters include airbrake deflection angle and angle of attack.

II. Experimental Technique

A. Model and Facility

Experiments have been performed on a 1:15-scale detailed steel model of a modern high-agility aircraft of the canard–delta-wing type

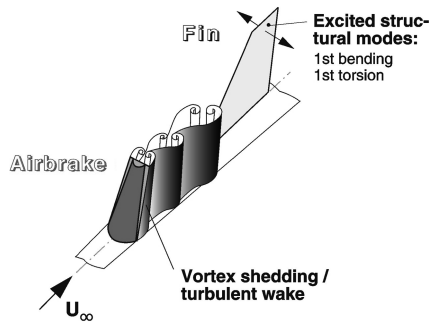

Fig. 2 Phenomenology of fin buffeting evoked by turbulent wakes shed at bluff bodies.

$2s = 0.740$ m	$l_\mu = 0.360$ m
$\Lambda_W = 2.45$	$\lambda_W = 0.14$
$\Lambda_F = 1.38$	$\lambda_F = 0.19$
$\varphi_W = 50°$	$\lambda_C = 0.33$
$\varphi_C = 45°$	$\varphi_F = 54°$

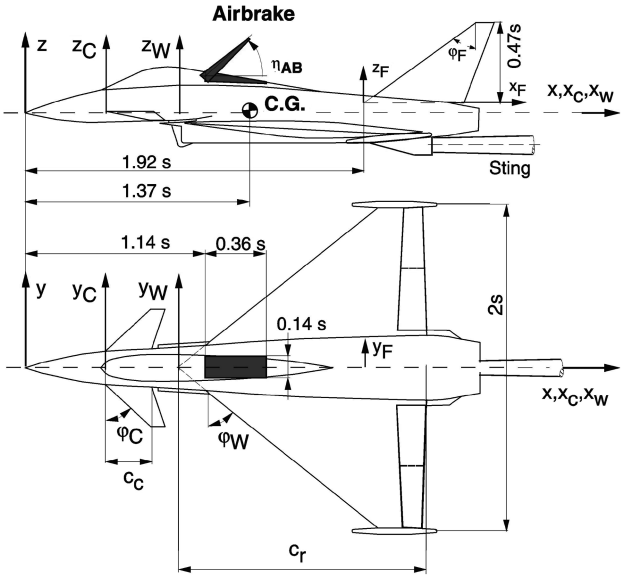

Fig. 3 Geometry of delta–canard configuration.

(Fig. 3). Major parts of the model are the nose section, front fuselage with rotatable canards and a single place canopy, center fuselage with delta wing and a throughflow double air intake underneath, and rear fuselage including nozzle section and vertical tail (fin). The air brake is located in the rear part of the canopy with a length of 0.36 and a width of 0.14 based on the wing semispan. The airbrake model consists of the deflected canopy fairing and the actuator sting (Fig. 4a). Because of the sharp side and upper edges of the air brake, it is assumed that flow separation is only slightly influenced by Reynolds number effects. The airbrake deflection angles studied include $\eta_{AB} = 45$ and 60 deg.

The experiments have been carried out in the low-speed wind-tunnel facility B of the Institute of Aerodynamics of Technische Universität München. This closed-return wind tunnel is operated with an open test section at the maximum usable velocity of 60 m/s. Test-section dimensions are 1.2 m in height, 1.55 m in width, and 2.8 m in length. The test-section flow was carefully inspected and calibrated, documenting a turbulence level of less than 0.4% and uncertainties in the spatial and temporal mean velocity distributions of less than 0.067%. The maximum blockage at the model incidence of $\alpha = 30$ deg is below 6%. The model is sting-mounted using a Z-shaped adapter for connection with the horizontal sting of the three-axis model support (Fig. 4b). The computer-controlled model support provides an angle-of-attack range of -10 deg $\leq \alpha \leq +30$ deg, and models may be yawed and rolled 360 deg. The uncertainty in angle setting is less than 0.05 deg.

B. Instrumentation and Test Conditions

The fin is instrumented with 18 differential unsteady pressure transducers (Kulite LQ-32-064 5 psi D) at 9 positions directly opposite each other on each surface. The sensor voltages of each channel are amplified for optimum signal levels, sampled with 2000 Hz, and low-pass-filtered at 256 Hz. The data of all channels are simultaneously recorded over a time interval of 30 s and digitized

a)

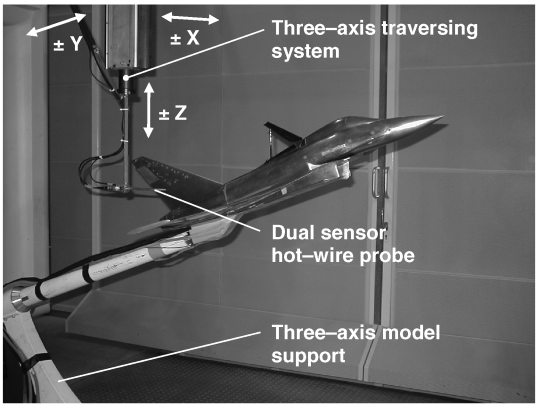

b)

Fig. 4 Model mounted in the test section: a) air brake and actuator sting (view from behind) and b) horizontal sting of three-axis model support and three-axis traversing system for hot-wire flowfield measurements.

with 14-bit precision. Thus, the sample block contains 60,000 values. Pressure-sensor sensitivities are specified by the manufacturer data sheets, the values of which are in the range of 15–17 mV/psi ($\approx$2 μV/Pa). These values are also proven by our own calibration. The pressure-signal resolution is then about 2 Pa regarding the measurement system voltage range of ($\pm$10 V), with digital accuracy of 14 bit, an amplification factor of 250, sensor sensitivities of approximately 2 μV/Pa, and a system accuracy of about 0.15%.

The time-dependent flowfield velocities are measured using advanced hot-wire anemometry. A three-axis traversing system is used to move a self-manufactured miniature cross-wire probe to the defined measurement points (Fig. 4b). These points are distributed over four crossflow planes located downstream of the air brake above the fuselage. Based on the wing half-span, the lateral and vertical distance of the measurement points is 0.013 in the inner and 0.027 in the outer area of the crossflow planes. The anemometer output voltages are sampled with 3000 Hz over 6.4 s and low-pass-filtered at 1000 Hz. The sample block of 19,200 values is digitized with 16-bit precision. The data acquisition parameters are based on previous tests to ensure that all significant flowfield phenomena are captured and on statistical accuracies of 1 and 2.5% for the root mean square (rms) values and spectral densities, respectively.

The measurements have been made at a freestream reference velocity of $U_\infty = 40$ m/s at ambient pressure p_∞ and ambient temperature T_∞. The corresponding Reynolds numbers based on the wing mean aerodynamic chord l_μ is $Re_{l_\mu} = 0.97 \times 10^6$. Consequently, turbulent boundary layers are present at wing and control surfaces. All control surfaces (namely, canard and leading-edge slats and trailing-edge flaps) are set to 0 deg. Flowfield surveys are conducted at angles of attack of $\alpha = 0$, 15, and 20 deg, and fin pressure fluctuations are taken in the range of 0 deg $\leq \alpha \leq$ 30 deg at an incidence step of $\Delta\alpha = 1$ deg.

III. Results and Discussion

A. Baseline Configuration

The flowfield of the delta–canard configuration is characterized by the presence and interaction of leading-edge and trailing-edge vortices. Leading-edge vortices start to develop at wing and canard surfaces already at low angles of attack. At $\alpha = 15$ deg, the wing leading-edge vortex is clearly depicted by the vector field of the crossflow velocities plotted here for two stations located at 40% ($x/c_r = 0.4$) and 100% ($x/c_r = 1.0$) wing root chord (Fig. 5a). Bursting of the wing leading-edge vortex occurs at $x/c_r \approx 0.4$, indicated by an enlarged core region of very low crossflow velocities. Vortex breakdown is caused by the adverse pressure gradient leading to stagnation of the axial core flow. Consequently, the vortex core diameter expands rapidly, accompanied by large fluctuation levels. The development of the delta-wing and canard vortex systems at $\alpha = 15$ deg is further sketched in Fig. 5b based on laser light sheet flow visualization. Except for the wing leading-edge vortices, the dominating vortices include also the canard leading-edge and trailing-edge vortices. Progressing downstream over the wing, the crossflow velocities of the wing leading-edge vortices move the canard vortices inboard and downward.

The unsteady fin flowfield is therefore mainly influenced by induction effects evoked by the wing and canard vortices. The lateral rms velocities provide a measure for the fluctuation intensity of the velocity component that is normal to the fin surface (Fig. 6). Downstream of vortex bursting, high turbulence intensities exist at

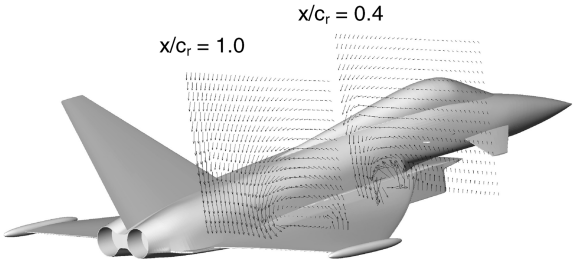

a)

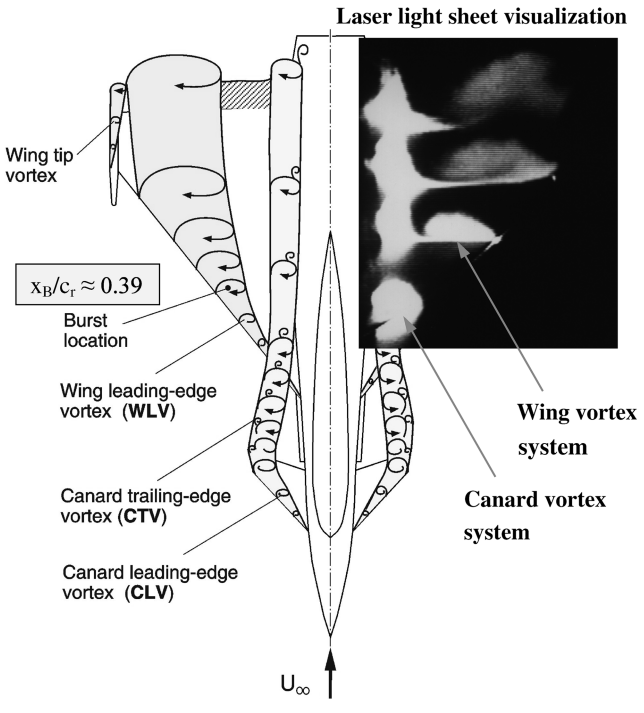

b)

Fig. 5 Flowfield characteristics of delta–canard configuration at α = 15 deg and $Re_{l_\mu} = 0.97 \times 10^6$: a) crossflow velocity vector fields at 40 and 100% root chord position and b) topology of main vortex systems.

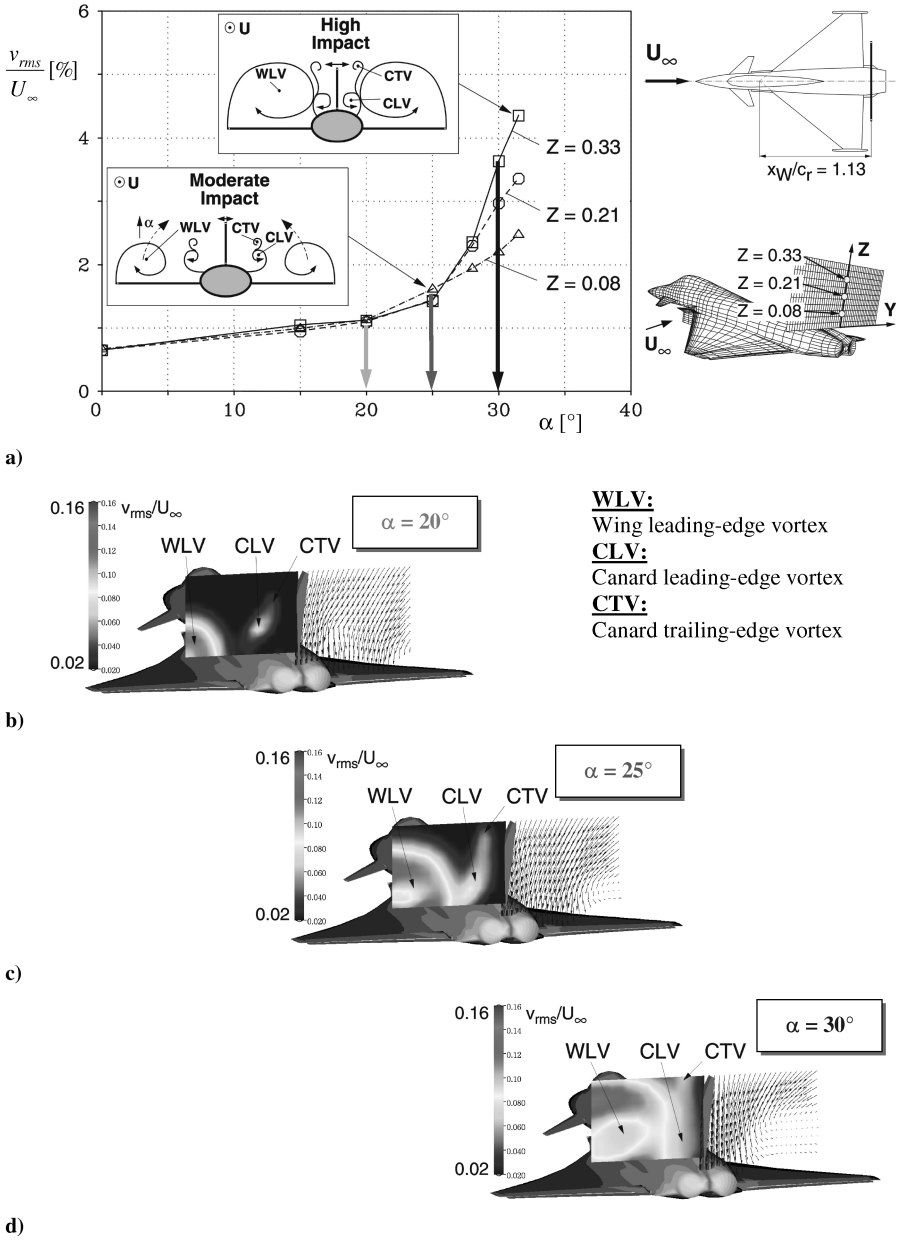

Fig. 6 Lateral rms velocities v_{rms}/U_∞ measured in the fin region and in a plane normal to the fin surface for various angles of attack, where $U_\infty = 40$ m/s and $Re_{l_\mu} = 0.97 \times 10^6$.

the points of inflection in the radial profiles of retarded axial core flow. Thus, an annular region of high-velocity fluctuations surrounds the expanded vortex core [14]. Those findings are also reported for investigations on a variety of generic delta-wing configurations [13]. Here, the levels of the lateral rms velocities in the fin region increase moderately up to angles of attack of $\alpha \approx 20$ deg. Up to this incidence, the fin flowfield is only slightly influenced by the highly turbulent flow attributed to the burst wing and canard vortices (Fig. 6b). This moderate impact is further depicted by the schematic of Fig. 6a based on flowfield measurements in a plane normal to the fin surface. Beyond $\alpha = 25$ deg, there is a steep rise in the rms level, indicating the strengthening induction of the approaching burst wing and canard vortices (Fig. 6c). The induction increases with angle of attack as the vortices move inboard and upward, accompanied by a strong enlargement of the core region of the burst vortices (Fig. 6d). Therefore, the areas of maximum turbulence intensities are shifted toward the symmetry plane, and the turbulence level at the centerline fin raises from moderate to high levels at a steep gradient.

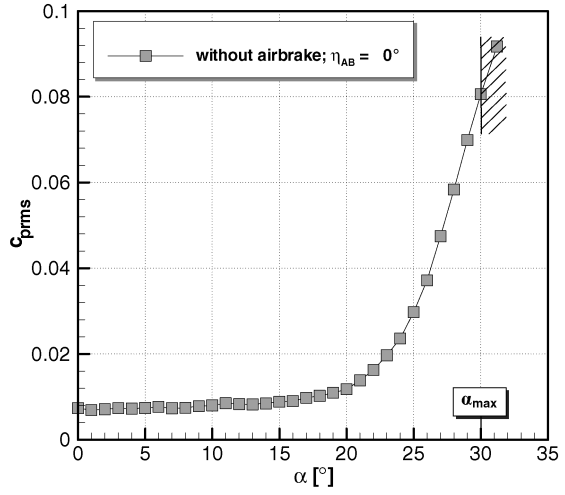

Fig. 7 Surface-averaged rms fin pressure coefficient $c_{p_{rms}}$ as a function of angle of attack α; $U_\infty = 40$ m/s and $Re_{l_\mu} = 0.97 \times 10^6$.

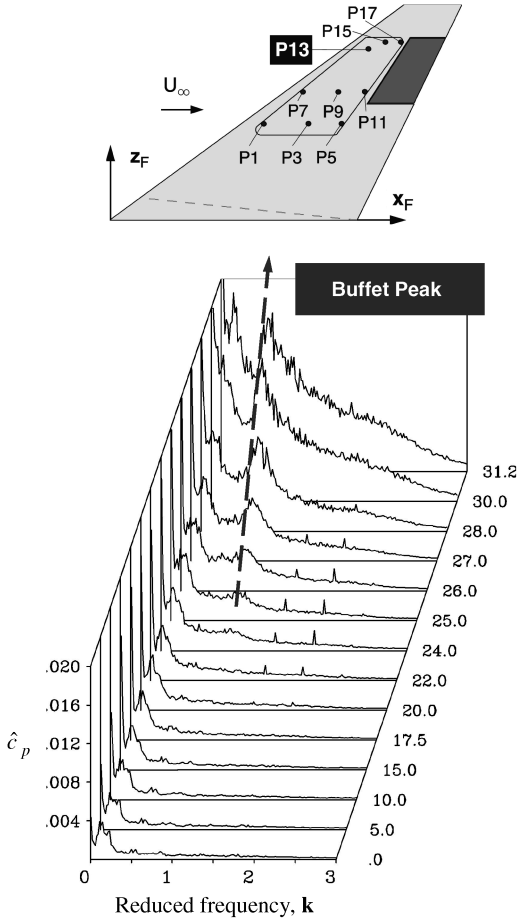

Fig. 8 Amplitude spectra of fluctuating fin-surface pressure coefficient for station P13 at $\alpha = 0$–31.2 deg; $U_\infty = 40$ m/s and $Re_{l_\mu} = 0.97 \times 10^6$.

The unsteady flowfield induces pressure fluctuations on the fin. The surface-averaged rms values of the fluctuations in the pressure coefficient are plotted as a function of angle of attack in Fig. 7. Representing the trend in the lateral turbulence intensities, the rms pressure coefficient increases significantly above $\alpha = 20$ deg, reaching a value of about 8% at a maximum angle of attack of $\alpha \approx 30$ deg. The severe increase in the rms pressure above a certain incidence is a characteristic feature of the fin-buffet phenomenon. It reflects the increasing influence of the burst wing and canard vortices, with their annular regions of maximum turbulence intensity approaching the midsection. The amplitude spectra of the fluctuating pressure coefficient, calculated from the signal taken at station P13, are shown in Fig. 8 for all angles of attack tested. Above $\alpha \approx 22$ deg, spectral peaks can be identified in the range of reduced frequencies of $k = 0.8$–0.6. The reduced frequency $k = f l_\mu / U_\infty$ is based on wing mean aerodynamic chord and freestream velocity. This energy peak, called the *buffet peak*, increases strongly with increasing angle of attack. Thus, the narrowband concentration of turbulent kinetic energy may result in strong excitation of structural modes.

It can be further detected that the associated reduced frequencies are shifted to lower values at higher angles of attack. This shift in the dominant reduced frequency is plotted in Fig. 9. The quasi-periodic velocity and induced surface pressure fluctuations, respectively, result from the helical-mode instability of the flow downstream of vortex breakdown [13,14]. The burst vortex core expands with increasing angle of attack and therefore the wavelength of the instability mode becomes larger and the corresponding frequency

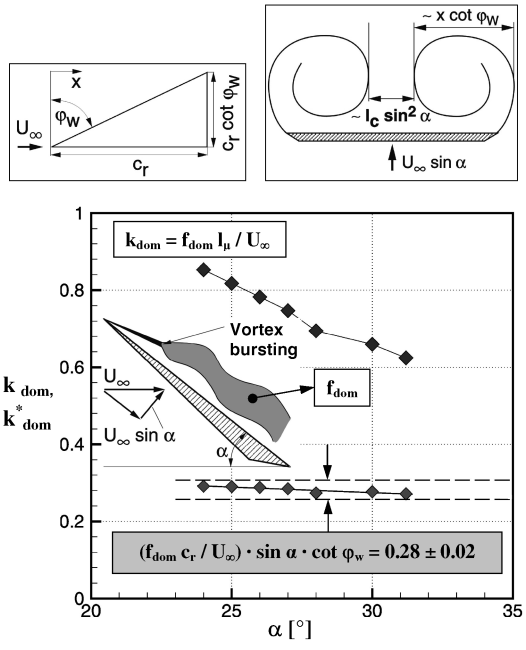

Fig. 9 Dominant reduced buffet frequency k_{dom} and k^*_{dom} as a function of angle of attack based on amplitude pressure spectra of fin station P13.

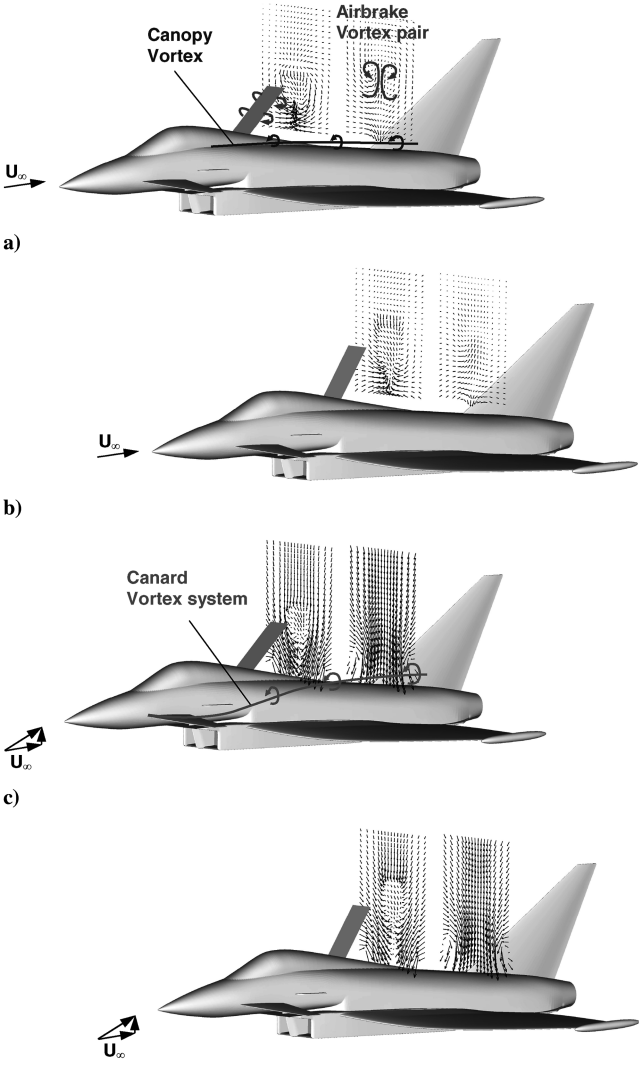

Fig. 10 Crossflow velocity vectors for two planes in the airbrake wake, where $U_\infty = 40$ m/s and $Re_{l_\mu} = 0.97 \times 10^6$: a) $\alpha = 0$ deg, $\eta_{\mathrm{AB}} = 45$ deg, b) $\alpha = 0$ deg, $\eta_{\mathrm{AB}} = 60$ deg, c) $\alpha = 15$ deg, $\eta_{\mathrm{AB}} = 45$ deg, and d) $\alpha = 15$ deg, $\eta_{\mathrm{AB}} = 60$ deg.

becomes smaller. A universal frequency parameter can be derived using appropriate scaling quantities. Referring to velocity, the component normal to the leading edge ($U_\infty \sin\alpha$) has to be considered. The length scale must account for the expansion of the burst vortex core, given approximately by the local half-span ($\sim x \cot\varphi_W$) and the shear-layer distance ($\sim \sin^2\alpha$). The root chord c_r is taken for the streamwise distance x to describe the vortex core expansion in the fin region (i.e., at the position of the wing trailing edge). Hence, for the scaled dominant reduced frequency k^*_{dom}, it results in

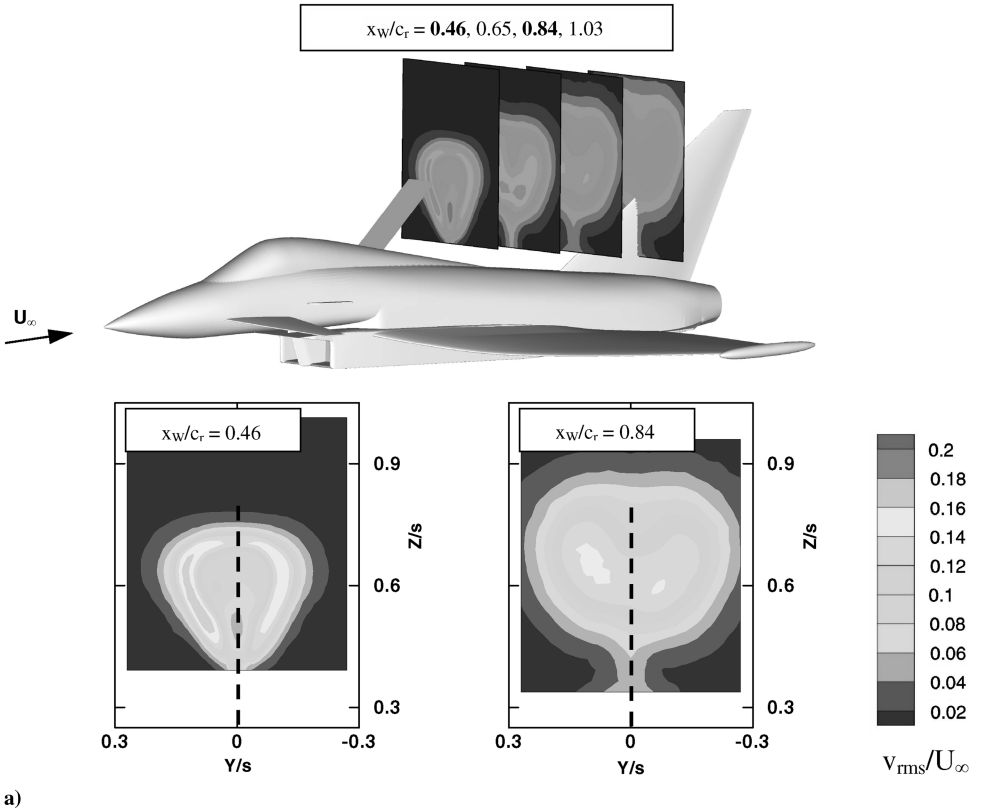

a)

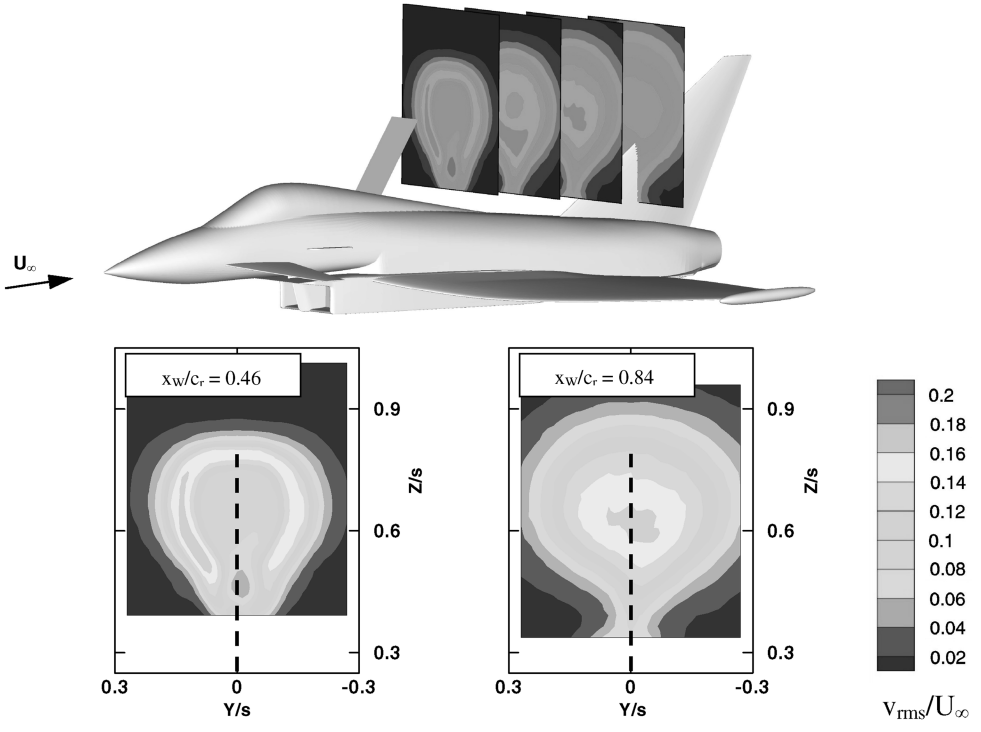

b)

Fig. 11 Turbulence-intensity distributions of the lateral velocity fluctuations $v_{\mathrm{rms}}/U_\infty$ for four crossflow planes in the airbrake wake, where $U_\infty = 40$ m/s and $Re_{l_\mu} = 0.97 \times 10^6$: a) $\alpha = 0$ deg, $\eta_{\mathrm{AB}} = 45$ deg, and b) $\alpha = 0$ deg, $\eta_{\mathrm{AB}} = 60$ deg.

$$k^*_{\mathrm{dom}} = \frac{f_{\mathrm{dom}} l_C}{U_C} = \frac{f_{\mathrm{dom}} x \cot\varphi_W \sin^2\alpha}{U_\infty \sin\alpha}$$
$$= \underbrace{\frac{f_{\mathrm{dom}} c_r}{U_\infty}}_{k_{\mathrm{dom}}\cdot(c_r/l_\mu)} \cot\varphi_W \sin\alpha = 0.28 \pm 0.02 \qquad (1)$$

Equation (1) leads to a scaling with the sine of angle of attack α and the cotangent of the wing leading-edge sweep φ_W. This scaling groups the values of the dominant reduced frequencies within a band of 0.28 ± 0.02. Evaluating the measurements on different configurations [5,6,12,18] substantiates the validity of the derived frequency parameter.

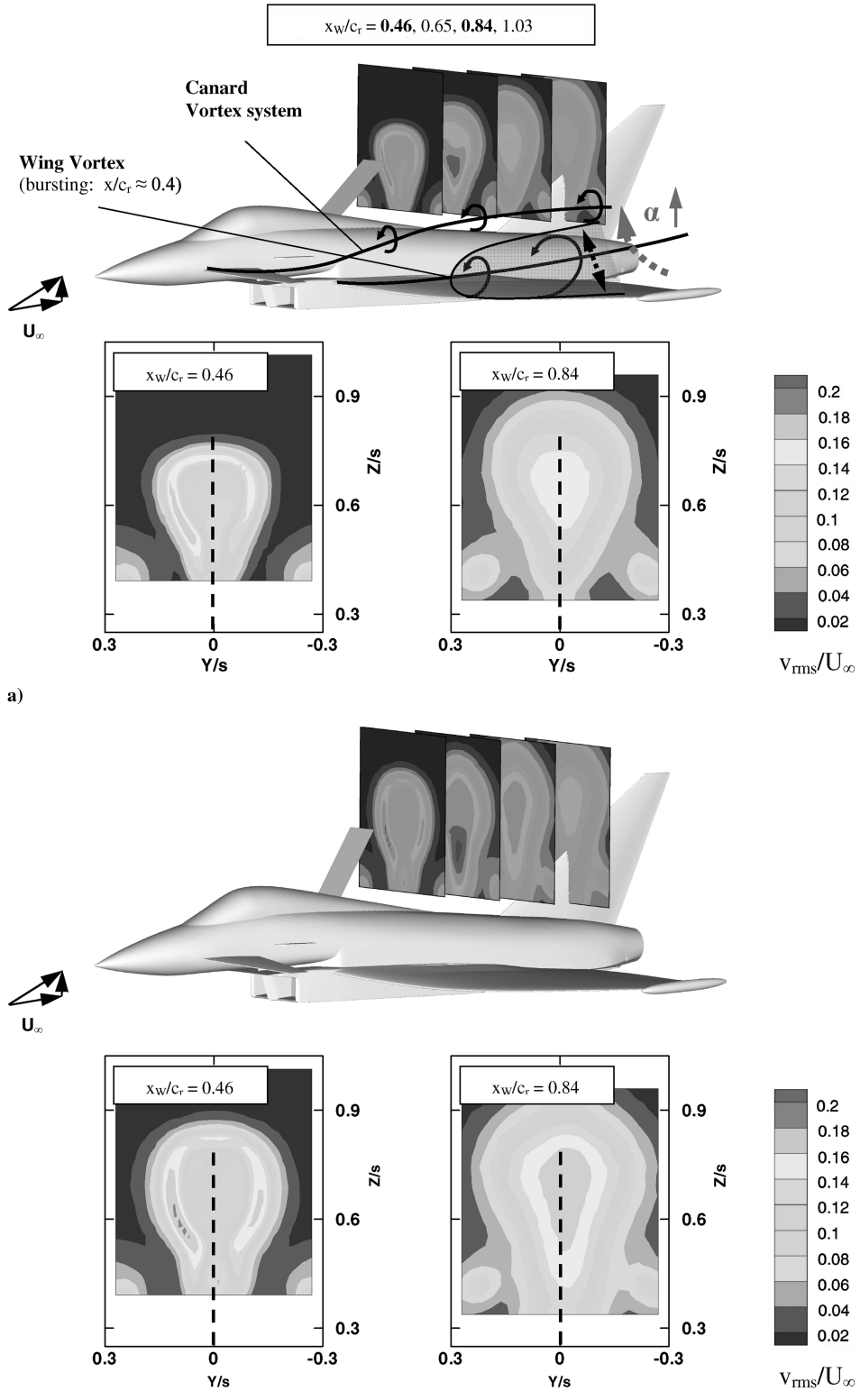

Fig. 12 Turbulence-intensity distributions of the lateral velocity fluctuations $v_{\mathrm{rms}}/U_\infty$ for four crossflow planes in the airbrake wake, where $U_\infty = 40$ m/s and $Re_{l_\mu} = 0.97 \times 10^6$: a) $\alpha = 15$ deg, $\eta_{\mathrm{AB}} = 45$ deg, and b) $\alpha = 15$ deg, $\eta_{\mathrm{AB}} = 60$ deg.

B. Airbrake Configuration

In comparison with the baseline configuration, the flowfields for the cases of deflected air brake are analyzed, showing specific phenomena superimposed on the baseline characteristics.

1. *Mean and Turbulent Flowfield*

The crossflow velocity vectors give an overview of the mean flowfield development in the airbrake wake for stations close behind the air brake and at the fin root (Fig. 10). Results are shown for both airbrake deflections of $\eta_{AB} = 45$ and 60 deg and for angles of attack of $\alpha = 0$ and 15 deg. The velocity components are based on a wind-tunnel fixed coordinate system. For the upstream station at $\alpha = 0$ deg (Figs. 10a and 10b), the mean velocities depict increased crossflow components directed toward the dead-water region behind the air brake. In the lower part of the symmetry plane, high crossflow velocities are present, with their vectors pointing inboard and upward. Flow separation at the airbrake edges results in a

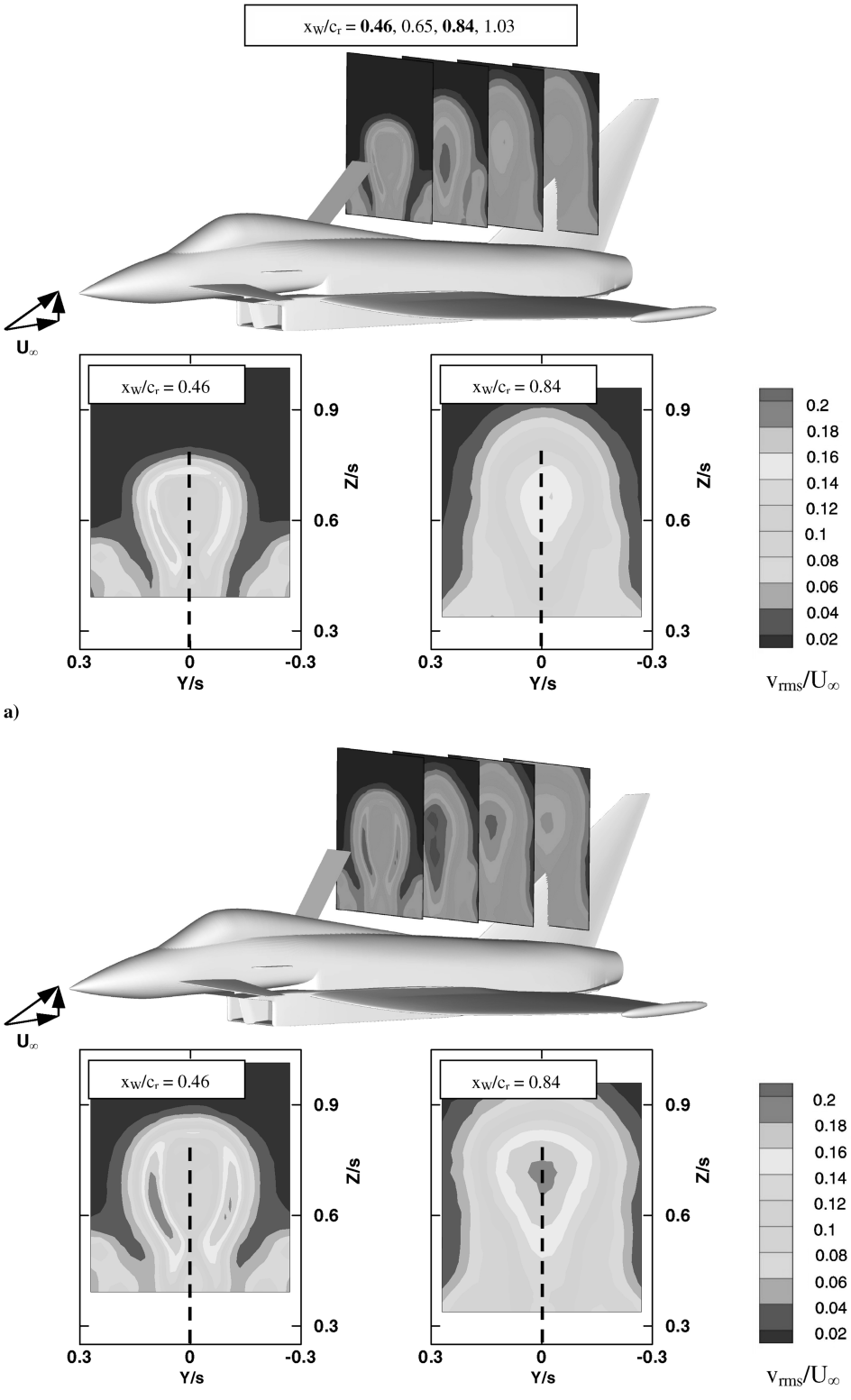

Fig. 13 Turbulence-intensity distributions of the lateral velocity fluctuations v_{rms}/U_∞ for four crossflow planes in the airbrake wake, where $U_\infty = 40$ m/s and $Re_{l_\mu} = 0.97 \times 10^6$: a) $\alpha = 20$ deg, $\eta_{AB} = 45$ deg, and b) $\alpha = 20$ deg, $\eta_{AB} = 60$ deg.

counter-rotating vortex pair that continues to exist downstream up to the fin region. A second vortex pair can be detected at the lower corners of the measurement planes, associated with flow separation at the canopy. The induced crossflow velocities, especially in the area above the fuselage, increase in strength with increasing angle of attack, and the airbrake wake becomes laterally compressed (Figs. 10c and 10d). At $\alpha = 15$ deg, a further vortex system dominates the lower outboard parts of the measurement planes. This vortex system is shed at the canard, consisting of the canard leading-edge vortex and trailing-edge vortex, the downstream development of which is sketched in Fig. 5.

The discussion of the unsteady flowfield focuses on the turbulence intensity of the lateral velocity fluctuations v_{rms}/U_∞. This flowfield pattern is shown in Fig. 11 for $\alpha = 0$ deg and $\eta_{\text{AB}} = 45$ and 60 deg. The shear layers emanating from the upper edge and the side edges of the air brake form a horseshoelike region of increased turbulence intensities. There, turbulence maxima occur in a limited radial range. At $\alpha = 0$ deg and $\eta_{\text{AB}} = 45$ deg, the rms maxima reach levels of about 16% of the freestream velocity. Downstream, the inboard-directed crossflow velocities push the areas of turbulence maxima together. Thus, an annular region of high-velocity fluctuations exists and determines the flowfield features in the symmetry plane at the fin location. Raising the airbrake deflection to $\eta_{\text{AB}} = 60$ deg enlarges the radial range of the region of increased turbulence intensities. This enlargement is also shown as a vertically extended area of maximum velocity fluctuations impinging on the fin. In addition to this spatial extension, higher turbulence levels are also present. The turbulence-intensity distributions at $\alpha = 15$ deg are included in Fig. 12. The canard vortex system reveals itself by circlelike areas of increased velocity fluctuations that are well separated from the airbrake wake. Downstream, the crossflow velocities induced by the canard vortices have the effect that the high-turbulence-intensity region at the fin is stretched in the direction of the fuselage. In addition, this region is compressed because of the inboard and upward movement and the radial expansion of the burst wing vortices with increasing angle of attack. Consequently, the region of maximum turbulence intensities covers nearly the whole height of the fin at $\eta_{\text{AB}} = 60$ deg. The influence of the canard and wing vortices becomes even stronger at $\alpha = 20$ deg (Fig. 13). On one hand, the velocity fluctuations attributed to the burst canard vortices raise the turbulence-intensity level in the root area of the fin. On the other hand, the incidence-dependent movement and expansion of the burst wing vortices further compresses the region of high turbulence intensities over the fin surface. Therefore, an absolute rms maximum is found near the fin tip, reflecting a high excitation level.

Further, the airbrake wake exhibits specific frequency-dependent concentrations of turbulent kinetic energy. This narrowband energy concentration is indicated by a distinct spike in the power spectral density distribution of the lateral velocity fluctuations. A typical example for such a spectral distribution is presented in Fig. 14 for a streamwise station just upstream of the fin at an angle of attack of $\alpha = 0$ deg. This result substantiates that the coherent turbulent structures shed at the airbrake edges are linked to a quasi-periodic vortex shedding.

2. *Pressure Fluctuations on the Fin Surface*

The unsteady velocities create pressure fluctuations on the fin that are again quantified by the surface-averaged rms values of the fluctuating part of the pressure coefficient $c_{p_{\text{rms}}}$ (Fig. 15). The reference basis is given by the results of the baseline configuration (cf. Fig. 7). Compared with the baseline, the configurations with deflected air brake, $\eta_{\text{AB}} = 45$ and 60 deg, show significantly higher rms values of pressure fluctuations up to $\alpha \approx 25$ deg. The pressure fluctuations on the fin surface become stronger with increasing airbrake deflection. But the differences in rms pressures between both deflections are small for low and moderate angles of attack. Also, the rms levels are nearly constant up to $\alpha \approx 12$ deg. These features are based on the similarity of the airbrake wake flow characterized by periodic vortex shedding and dominating crossflow, also depicted by smoke visualization of the airbrake wake. For $\alpha > 12$ deg, the decrease in effective airbrake deflection angle with increasing angle of attack becomes relevant. The vortical structures emanating from the airbrake side edges change from a vertical to an axial orientation. Therefore, the bluff-body wake with periodic vortex shedding transforms into the wake of burst leading-edge vortices, depicted again by smoke visualization. In addition, the airbrake wake is strongly influenced by the expansion of the burst wing vortices and induction effects of the canard vortices. Consequently, the significant raise in rms pressures with angle of attack is shifted to a lower angle of attack than with the baseline, and it starts here at $\alpha \approx 12$ deg. At high angles of attack, $\alpha > 25$ deg, the effective airbrake incidence becomes so small that no significant vortex formation at the side edges takes place. The unsteady pressure characteristics then follow the trend of the baseline configuration. The pressure-fluctuation intensities at certain sensor positions reach

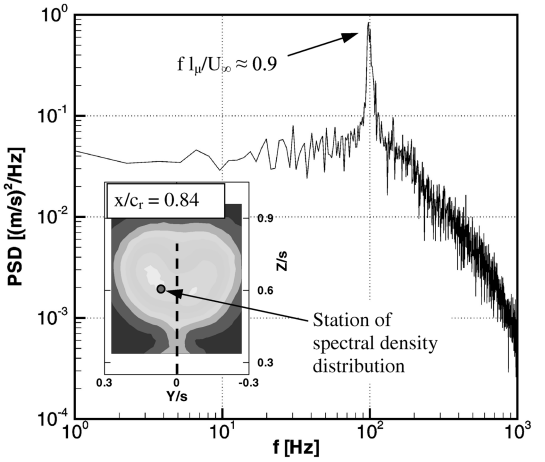

Fig. 14 Spectral density distribution of lateral velocity fluctuations at $x/c_r = 0.84$, $\alpha = 0$ deg and $\eta_{\text{AB}} = 45$ deg; $U_\infty = 40$ m/s and $Re_{l_\mu} = 0.97 \times 10^6$.

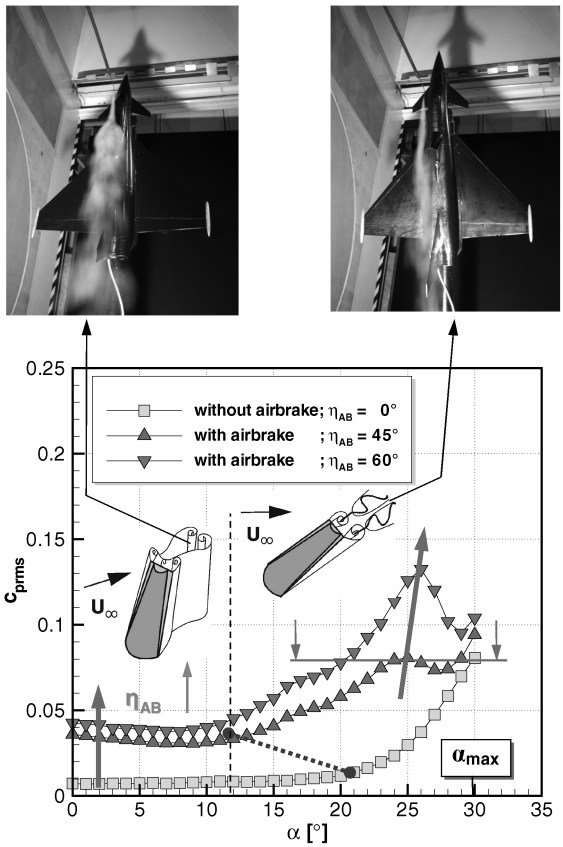

Fig. 15 Surface-averaged rms fin pressure coefficient $c_{p_{\text{rms}}}$ as a function of angle of attack α for airbrake deflections of $\eta_{\text{AB}} = 45$ and 60 deg; $U_\infty = 40$ m/s and $Re_{l_\mu} = 0.97 \times 10^6$.

levels that are 2 times higher than the surface-averaged values. A reduction of the airbrake deflection from $\eta_{AB} = 60$ to 0 deg within the angle-of-attack range of $\alpha = 20$ to 25 deg avoids these peak values of surface pressure-fluctuation intensities. It would ensure that the dynamic loads do not exceed the limiting values of the baseline configuration given by maximum angle-of-attack conditions.

3. Characteristics of Reduced Frequencies

In addition to the intensity of the pressure fluctuations, the frequency characteristics are of particular interest with respect to the excitation of structural modes. Power spectral densities of the surface pressure fluctuations are calculated to analyze narrowband energy concentrations and to determine dominant reduced frequencies and

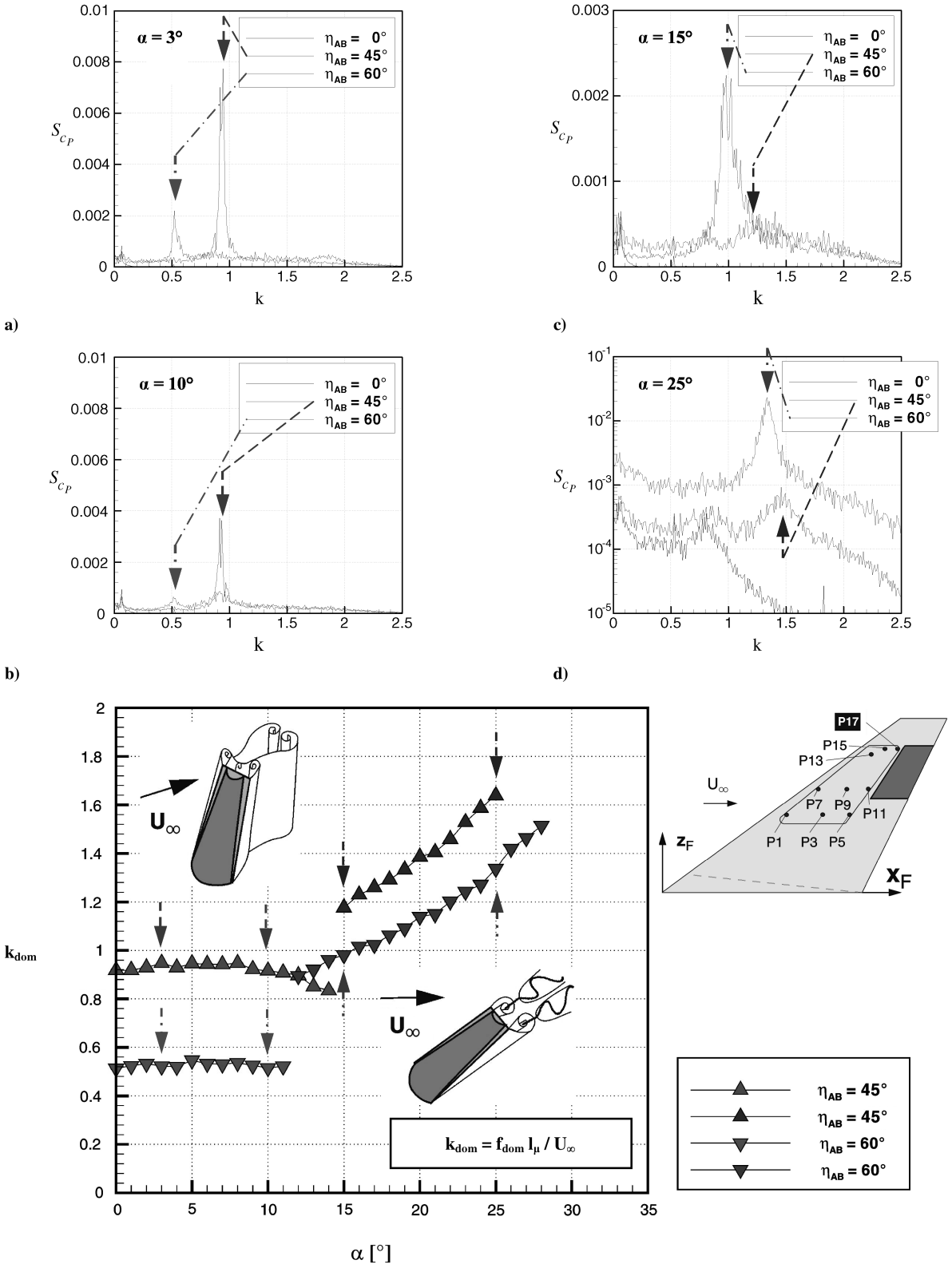

Fig. 16 Power spectral densities of fin-surface pressure fluctuations S_{c_p} taken at station P17 for airbrake deflections of $\eta_{AB} = 45$ and 60 deg: a–d) angles of attack and e) dominant reduced frequencies k_{dom} as a function of angle of attack; $U_\infty = 40$ m/s and $Re_{l_\mu} = 0.97 \times 10^6$.

dependencies on angle of attack. Results are shown for the sensor station P17 (Fig. 16). At low and moderate angles of attack (here, $\alpha = 3$ and 10 deg), the periodic vortex shedding results in strong spectral density peaks. The dominant reduced frequencies based on freestream velocity and wing mean aerodynamic chord show higher values for $\eta_{AB} = 45$ deg than for $\eta_{AB} = 60$ deg. For both cases, the reduced frequencies are nearly constant over the angle-of-attack range of $\alpha = 0$–12 deg, again demonstrating the similarity of airbrake vortex shedding in this incidence range. The characteristic of the reduced frequency versus angle of attack changes for $\alpha >$ 12 deg when airbrake side-edge vortices transform to leading-edge vortices due to the decrease in the side-edge inclination. The turbulent-energy concentration is shifted to higher reduced frequencies, the values of which increase with increasing angle of attack, because the airbrake incidence becomes reduced. Beyond an angle of attack of $\alpha \approx 25$ deg, vortex formation at the air brake disappears. The helical-mode instability of the burst wing vortices dominate the unsteady characteristics of the fin-surface pressure fluctuations, as found already for the baseline configuration (cf. Figure 9).

An appropriate scaling, taking into account a length scale based on shear-layer distances as well as a characteristic velocity regarding airbrake deflection and angle of attack, results in the scaling relations documented in Fig. 17. The reduced-frequency relation for the angle-of-attack range of $\alpha = 0$–12 deg is then given by

$$k^*_{dom} = \left(\frac{f_{dom} l_\mu}{U_\infty}\right)\left(\frac{d_{AB}}{l_\mu}\right)\tan\eta_{AB} = k_{dom}\left(\frac{d_{AB}}{l_\mu}\right)\tan\eta_{AB} = 0.20 \pm 0.005 \quad (2)$$

Here, the effective velocity normal to the airbrake side edges ($U_\infty \cot\eta_{AB}$) is used as the characteristic velocity and the airbrake width d_{AB} is used as a measure for the shear-layer distance. Thus, the dominant reduced frequencies show a nearly uniformly characteristic value of $k^*_{dom} \approx 0.2$, representing the case of periodic vortex shedding. This value matches with the well-known characteristic Strouhal number

$$Sr = \frac{f l_C}{U_C} = 0.198\left(1 - \frac{19.7}{Re}\right)$$

for a von Kármán vortex street [27] within a Reynolds number range of $250 < Re < 2 \times 10^5$. For the present case, the Reynolds number based on the airbrake width is about $Re_{d_{AB}} = 1.3 \times 10^5 \div 1.5 \times 10^5$.

The influence of the angle of attack in the effective normal velocity becomes dominant above $\alpha \approx 12$ deg. Therefore, Eq. (2) is changed as follows:

$$k^*_{dom} = k_{dom}\left(\frac{d_{AB}}{l_\mu}\right)\tan(\eta_{AB} - \alpha) = 0.28 \pm 0.01 \quad (3)$$

The characteristic value of $k^*_{dom} \approx 0.28$ corresponds to the dominant reduced frequency of the helical-mode instability, as explained for the burst wing vortices. These characteristic reduced-frequency values may serve as design quantities to judge the frequencies of the highest excitation levels for fin-buffet loads caused by a centerline air brake.

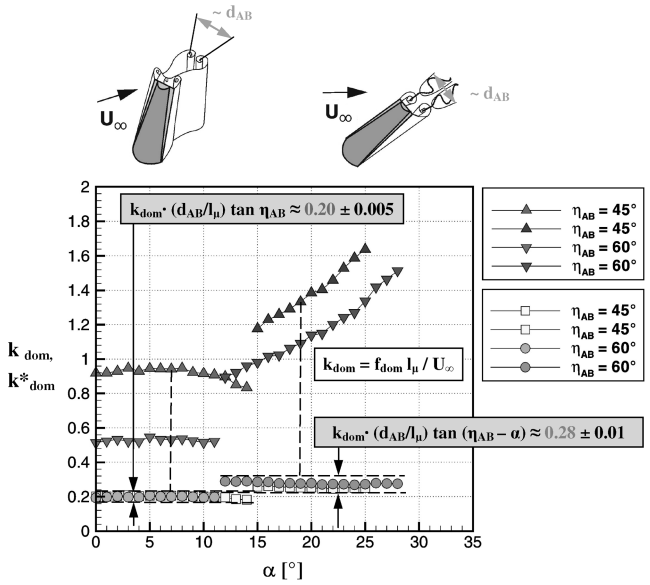

Fig. 17 Dominant reduced buffet frequency k_{dom} and k^*_{dom} as a function of angle of attack based on power spectral densities of pressure fluctuations taken at fin station P17.

IV. Conclusions

Flowfield and surface pressure measurements were performed to study the influence of a deflected air brake on the buffet characteristics of a vertical tail (fin). The results are based on wind-tunnel studies conducted on an 1:15-scale detailed model of a high-agility aircraft of the canard–delta-wing type fitted with a single fin. The air brake is located upstream at the rear part of the canopy. The main results of these investigations are as follows:

1) The fin-buffet environment of the baseline configuration (i.e., no airbrake deflection) is dominated by the burst wing and canard leading-edge vortices. Their impact leads to a strong increase in unsteady loads above $\alpha \approx 20$ deg, with a significant narrowband concentration of velocity and surface pressure fluctuations.

2) Compared with the baseline case, the airbrake wake causes unsteady aerodynamic loads on the fin already at low and moderate angles of attack. The levels of the airbrake-induced loads are 4 to 5 times higher than those of the baseline and increase with increasing airbrake deflection.

3) The fin-surface pressure fluctuations show three characteristic sections, depending on the angle of attack: up to $\alpha \approx 12$ deg, there is a nearly constant rms level, along with a constant reduced frequency due to quasi-periodic vortex shedding, creating large-scale coherent turbulent structures. From $\alpha \approx 12$ to 25 deg, the rms levels raise strongly. The vortices shed at the airbrake side edges transform into leading-edge vortices that burst downstream. The associated dominant reduced frequencies increase continuously with increasing angle of attack as the effective airbrake deflection angle is reduced. Above $\alpha \approx 25$ deg, the airbrake-induced unsteady loads diminish to the levels of the baseline. The formation of vortices at the airbrake side edges has stopped because the effective airbrake incidence becomes too small at high α. The unsteady loads are then dominated by the flowfield of the burst wing vortices.

4) Appropriate scaling quantities are introduced to derive characteristic reduced-frequency values k^*_{dom} for airbrake-induced fin-buffet loads. A value of $k^*_{dom} \approx 0.2$ is attributed to the case of periodic vortex shedding that occurs up to $\alpha \approx 12$ deg. Above that angle of attack, a value of $k^*_{dom} \approx 0.28$ holds for the case of axial-orientated burst vortices.

The results obtained contribute to setting up a database for design and evaluation purposes, focusing on unsteady aerodynamic loads. Further analysis will be carried out on the turbulent-flow structures and on the scaling of the quantities to extrapolate the results to full-scale aircraft.

Acknowledgment

The support of the investigations by the EADS Deutschland, GmbH, Military Aircraft Systems (MAS-MEG6) is gratefully acknowledged.

References

[1] Bisplinghoff, R. L., Ashley, H., and Halfman, R. L., "*Aeroelasticity*," Dover, Mineola, NY, 1996.

[2] Fung, Y. C., *An Introduction to the Theory of Aeroelasticity*, Dover, New York, 2002.
[3] Luber, W., Becker, J., and Sensburg, O., "The Impact of Dynamic Loads on the Design of Military Aircraft," *Loads and Requirements for Military Aircraft*, AGARD Rept. AGARD-R-815, Neuilly-sur-Seine, France, Sept. 1996, pp. 8-1–8-27.
[4] Del Frate, J. H., and Zuniga, F. A., "In-Flight Flow Field Analysis on the NASA F-18 High Alpha Research Vehicle with Comparisons to Ground Facility Data," AIAA Paper 90-0231, Jan. 1990.
[5] Ferman, M. A., Patel, S. R., Zimmermann, N. H., and Gerstenkorn, G., "A Unified Approach to Buffet Response of Fighter Aircraft Empennage," *Aircraft Dynamic Loads due to Flow Separation*, AGARD Rept. AGARD-CP-483, Neuilly-sur-Seine, France, Apr. 1990, pp. 1-1–1-26.
[6] Lee, B. H. K., "Vertical Tail Buffeting of Fighter Aircraft," *Progress in Aerospace Sciences*, Vol. 36, Nos. 3–4, 2000, pp. 193–279. doi:10.1016/S0376-0421(00)00003-8
[7] Breitsamter, C., and Laschka, B., "Fin Buffet Pressure Evaluation Based on Measured Flowfield Velocities," *Journal of Aircraft*, Vol. 35, No. 5, 1998, pp. 806–815.
[8] Özgören, M., Sahin, B., and Rockwell, D., "Vortex Structure on a Delta Wing at High Angle of Attack," *AIAA Journal*, Vol. 40, No. 2, 2002, pp. 285–292.
[9] Hummel, D., "On the Vortex Formation over a Slender Wing at Large Angles of Incidence," *High Angle of Attack Aerodynamics*, AGARD Rept. AGARD-CP-247, Neuilly-sur-Seine, France, Oct. 1978, pp. 15-1–15-17.
[10] Hummel, D., "Effects of Boundary Layer Formation on the Vortical Flow Above Slender Delta Wings," *Enhancement of NATO Military Flight Vehicle Performance by Management of Interacting Boundary Layer Transition and Separation*, NATO Rept. RTO-MP-AVT-111, Oct. 2004.
[11] Wedemeyer, E., "Vortex Breakdown," *High Angle of Attack Aerodynamics*, AGARD Rept. LS-121, Neuilly-sur-Seine, France, Mar. 1982, pp. 9-1–9-17.
[12] Gursul, I., and Xie, W., "Buffeting Flows over Delta Wings," *AIAA Journal*, Vol. 37, No. 1, 1999, pp. 58–65.
[13] Gursul, I., "Review of Unsteady Vortex Flows over Slender Delta Wings," *Journal of Aircraft*, Vol. 42, No. 2, 2005, pp. 299–319. doi:10.2514/1.5269
[14] Breitsamter, C., and Laschka, B., "Turbulent Flow Structure Associated with Vortex-Induced Fin Buffeting," *Journal of Aircraft*, Vol. 31, No. 4, 1994, pp. 773–781. doi:10.2514/3.46560
[15] Canbazoglu, S., Lin, J. C., Wolfe, S., and Rockwell, D., "Buffeting of Fins: Distortion of Incident Vortex," *AIAA Journal*, Vol. 33, No. 11, 1995, pp. 2144–2150. doi:10.2514/3.12959
[16] Özgören, M., Sahin, B., and Rockwell, D., "Perturbations of a Delta Wing: Control of Vortex Breakdown and Buffeting," *Journal of Aircraft*, Vol. 38, No. 6, 2001, pp. 1040–1050.
[17] Kim, Y., Rockwell, D., and Liakopoulos, A., "Vortex Buffeting of Aircraft Tail: Interpretation via Proper Orthogonal Decomposition," *AIAA Journal*, Vol. 43, No. 3, 2005, pp. 550–559. doi:10.2514/1.9989
[18] Meyn, L. A., and James, K. D., "Full-Scale Wind Tunnel Studies of F/A–18 Tail Buffet," *Journal of Aircraft*, Vol. 33, No. 3, 1996, pp. 589–595. doi:10.2514/3.46986
[19] Kandil, O. A., Massey, S. J., Kandil, H. A., "Computations of Vortex-Breakdown Induced Tail Buffet Undergoing Bending and Torsional Vibrations," AIAA Paper 1994-1428, April 1994.
[20] Sheta, E. F., and Huttsell, L. J., "Numerical Analysis of F/A–18 Tail Buffet," AIAA Paper 2001-1664, April 2001.
[21] Morton, S., McDaniel, D., and Cummings, R., "F-16XL Unsteady Simulations for the CAWAPI Facet of RTO Task Group AVT-113," AIAA Paper 2007-493, Jan. 2007.
[22] Ferman, M. A., Liguore, S. L., Smith, C. M., and Colvin, B. J., "Composite 'Exoskin' Doubler Extends F-15 Vertical Fatigue Life," AIAA Paper 93-1341, Apr. 1993.
[23] Hebbar, S. K., Platzer, M. F., and Frink, W. D., "Effect of Leading-Edge Extension Fences on the Vortex Wake of an F/A–18 Model," *Journal of Aircraft*, Vol. 32, No. 3, 1995, pp. 680–682. doi:10.2514/3.46774
[24] Galea, S. C., Ryall, T. G., Henderson, D. A., Moses, R. W., White, E. V., and Zimcik, D. G., "Next Generation Active Buffet Suppression System," AIAA Paper 2003–2905, July 2003.
[25] Sheta, E. F., "Alleviation of Vertical Tail Buffeting of F/A–18 Aircraft," *Journal of Aircraft*, Vol. 41, No. 2, 2004, pp. 322–330. doi:10.2514/1.9327
[26] Breitsamter, C., "Aerodynamic Active Control for Fin-Buffet Load Alleviation," *Journal of Aircraft*, Vol. 42, No. 5, 2005, pp. 1252–1263. doi:10.2514/1.8174
[27] Roshko, A., "On the Development of Turbulent Wakes from Vortex Streets," NACA, Rept. 1191, 1954.
[28] Roshko, A., "On the Wake and Drag of Bluff Bodies," *Journal of the Aeronautical Sciences*, Vol. 22, 1955, pp. 124–132.
[29] Bradbury, L., "Measurements with a Pulsed-Wire and a Hot-Wire in the Highly Turbulent Wake of a Normal Plate," *Journal of Fluid Mechanics*, Vol. 77, 1976, pp. 473–497. doi:10.1017/S0022112076002218
[30] Ozono, S., "Flow Control of Vortex Shedding by a Short Splitter Plate Asymmetrically Arranged Downstream of a Cylinder," *Physics of Fluids*, Vol. 11, No. 10, 1999, pp. 2928–2934.